Microchimica Acta (2025) 192:739
https://doi.org/10.1007/s00604-025-07608-w

RESEARCH

Structural influences on lattice distortion in luminescence finetuning of core–multi-shell upconversion nanoparticles highly doped with Yb^{3+} and Ho^{3+} ions

Qiqi Ji[1] · **Mengru Qin**[2] · **Tingting Zhu**[1] · **Yanshuang Jiang**[1] · **Yi Qu**[2] · **Yufeng Wang**[2] · **Guangli Shi**[3] · **Chenghao Piao**[4] · **Ye Zhang**[5] · **Dongli Qi**[1] · **Ye Kuang**[6] · **Longhai Shen**[1] · **Yiwei Wang**[2,7]

Received: 31 July 2025 / Accepted: 27 September 2025

Abstract

Core–multi-shell upconversion nanoparticles (UCNPs) highly doped with sensitizers and activators were synthesized by co-precipitation methods. With Zn^{2+} separately doped with Yb^{3+} or Ho^{3+} ions in different core–multi-shell structures, the nanoparticle morphologies, diffraction peak shifts, variations of upconversion luminescence (UCL) intensity and lifetime, underlying energy mechanisms, as well as multifunction potentials, were characterized and analyzed in detail. Lattice distortion promotes Yb^{3+} and Ho^{3+} 4f–4f transitions, but co-doping Gd^{3+} and Zn^{2+} ions in the $NaHoF_4$ matrix may induce offset of lattice distortion and lengthen the overall Yb^{3+}–Ho^{3+} energy transfer distance. Zn^{2+}-induced F^- vacancies can also quench energy as inner defects. And even in layers with identical content, the optimal Zn^{2+} doping can change with multi-shell structures. Besides, UCL intensity and lifetime may be non-positively correlated, especially in highly doped UCNPs with Zn^{2+} doping and multi-shell structures. With core-doped Zn^{2+} hetero-ions and controlled Yb^{3+} concentration, $NaGdF_4$:Yb^{3+}@$NaHoF_4$@$NaGdF_4$:Yb^{3+} structures can achieve lifetimes as high as 635.82 μs; while with core- or shell-doped Zn^{2+} hetero-ions, $NaHoF_4$@$NaHoF_4$@$NaGdF_4$:Yb^{3+}@$NaGdF_4$:Yb^{3+} structures can achieve comparable UCL intensities with varied lifetimes ranging from 111.58 to 245.29 μs. Multifunction characterizations manifested the high application potential of designed UCNPs in photo-induced bio-imaging and as contrast agents for both computed tomography and T_1/T_2-weighed magnetic resonance imaging. Our work can deepen the theory study of UCL finetuning with lattice distortion, and widen the multifunction application of $NaHoF_4$-based nanomaterials.

Keywords Upconversion nanoparticles · Lattice distortion · Highly doped · Core–multi-shell · $NaHoF_4$ · Magnetic resonance imaging

---

Qiqi Ji and Mengru Qin contributed equally.

✉ Dongli Qi
qidongli@sylu.edu.cn

✉ Ye Kuang
kuangye@sylu.edu.cn

✉ Longhai Shen
shenlonghai@sylu.edu.cn

✉ Yiwei Wang
wangyiwei@symc.edu.cn

[1] College of Science, Shenyang Ligong University, Shenyang 110159, PR China

[2] Department of Molecular Morphology Laboratory, School of Basic Medicine, Shenyang Medical College, Shenyang 110034, PR China

[3] Zolix Instruments Co., Ltd, Beijing 101102, PR China

[4] Radiology Department, the Second Affiliated Hospital of Shenyang Medical College, Shenyang 110035, China

[5] The First Laboratory of Cancer Institute, the First Hospital of China Medical University, Shenyang 110001, China

[6] College of Materials Science and Engineering, Shenyang Ligong University, Shenyang 110159, PR China

[7] Liaoning Province Key Laboratory for Phenomics of Human Ethnic Specificity and Critical Illness, Shenyang Medical College, Shenyang 110034, PR China

Introduction

Upconversion nanoparticles (UCNPs) doped with rare earth (RE) have attracted great attention as a new generation of luminescence material. Compared with quantum dots and organic dyes, the low toxicity [1], high stability [2], easy synthesis [3] of UCNPs, and large Stokes shift [4], narrow peak width [5], reduced photobleaching [6] of their upconversion luminescence (UCL), enable broad application prospects ranging from bioimaging [7, 8], anti-counterfeiting [9, 10] to sensing [11, 12]. Among these UCNPs, sensitizer (Yb^{3+}) and activator (Ho^{3+}, Er^{3+}, Tm^{3+}) highly doped ones, have been endowed with unique UCL properties such as exceptional brightness [13, 14], single-band emission [15, 16] and tunable lifetimes [17, 18]. Relevant UCL-finetuning strategies, mainly including lattice manipulation [19], inert or active shell coating [20–23], high excitation power density [24] and homogeneous doping [25], can effectively suppress the detrimental energy quenching in highly doped UCNPs and improve their UCL performances.

Lattice distortion raised by ionic radius discrepancies of dopants, can lower the crystal field symmetry around RE^{3+} ions to promote their 4f–4f transition abilities [26, 27]. Generally recognized and frequently adopted as it has been, lattice manipulation via chemical co-doping of hetero-ions (Li^{+}, Zn^{2+}, Fe^{3+}, etc.) [28–33] lacks insightful study in its relationship with core-multi-shell structures. Since sensitizers and activators are co-doped in conventional UCNPs such as the $NaYF_4$:Yb^{3+},Ho^{3+} and $NaGdF_4$:Yb^{3+},Er^{3+} structure [34, 35], it is also difficult to investigate the separate lattice distortion effects on sensitizers and activators. Besides, the strategy of hetero-ion doping has rarely been utilized in highly doped UCNPs. Targeted explorations on these issues are a necessity.

As one of the common UCL activators [36, 37], Ho^{3+} ions also possess short electronic relaxation time, high effective magnetic moment and high attenuation characteristic [38–41], so $NaHoF_4$-based nanomaterials can serve both as UCL emitters for bioimaging and as contrast agents for magnetic resonance imaging. With the trials by us and other researchers [42–44], the UCL of $NaHoF_4$ UCNPs has been achieved and developed, paving a solid path towards multifunction. Furthermore, the $NaHoF_4$@$NaGdF_4$:Yb^{3+} core–multi-shell structures facilitate UCL studies impossible or difficult to implement in conventional UCNPs, for example, UCL finetuning by doping Ce^{3+} ions only with activators or sensitizers [45, 46]. Therefore, these $NaHoF_4$-based core–multi-shell UCNPs have crucial scientific values in multifunctional application and UCL theory analysis.

Herein, through layer-by-layer method using RE chlorides and oleates, series of core-multi-shell UCNPs were synthesized, with Ho@Yb (highly doped Ho^{3+} ions in core and inner shells, while highly doped Yb^{3+} ions in outer shells, similarly hereinafter) or Yb@Ho characteristics. Zn^{2+} ions were doped in different layers for integrated research of structural influences on UCL intensity and lifetime finetuning operated by lattice distortion, lattice distortion in highly doped UCNPs, and separate lattice distortion influences on sensitizers and activators. Possible lattice distortion offset, changes of energy transfer efficiency in $NaHoF_4$:Gd^{3+} structures, energy quenching mechanisms of Zn^{2+}-induced inner defects, relationship between UCL intensity and lifetimes, and multifunctional application potentials of Zn^{2+}-doped Ho@Yb UCNPs were also discussed, and Zn^{2+} doping strategies in different structures were optimized. This research can provide theory directions for hetero-ion doping in core-multi-shell structures and add to the application prospects of $NaHoF_4$-based materials.

Sizes and morphologies of UCNPs

By the oleate route, multiple-shell UCNPs were synthesized layer by layer. Transmission electron microscope (TEM) images and size distribution diagrams of selected core-only, core–shell, core–double-shell and core–triple-shell UCNPs were shown in Fig. 1 and S1–S6. The samples were spherical and uniformly distributed. Respective size ranges were calculated to be 11–12, 18–20, 25–28 and 30–33 nm, so the first, second and third shells (S_1, S_2 and S_3) had average thicknesses of 3–4, 3–4 and 2–3 nm (Fig. 1j), respectively. Sample sizes were not much influenced by Zn^{2+} doping and different structures.

Apart from size growth, the core–multi-shell structures can also be directly identified by high-resolution TEM and elemental mapping images (see Fig. S7, S8 and relevant analysis). These results confirmed the solid synthesis of differently-structured UCNPs with Zn^{2+} doping.

Peak shifts in XRD patterns

In Bragg's Law of $2d\sin\theta = n\lambda$, d is the interplanar spacing, θ is the angle between the incident X-ray and the corresponding crystal plane, n is an integer and λ is the X-ray wavelength [47]. Therefore, when ions with larger or smaller ionic radii are doped, d expands or shrinks to cause θ to decrease or increase, and X-ray diffraction (XRD) peaks shift to lower or higher angles, respectively.

As shown in Fig. 2 andS9–S16, all diffraction peaks of synthesized samples can be well indexed to β-$NaHoF_4$ (JCPDS-49–1896), proving the single hexagonal phase without purities. In zoomed-in figures, shifts of the selected (201) peak can be observed, as has been analysed in our

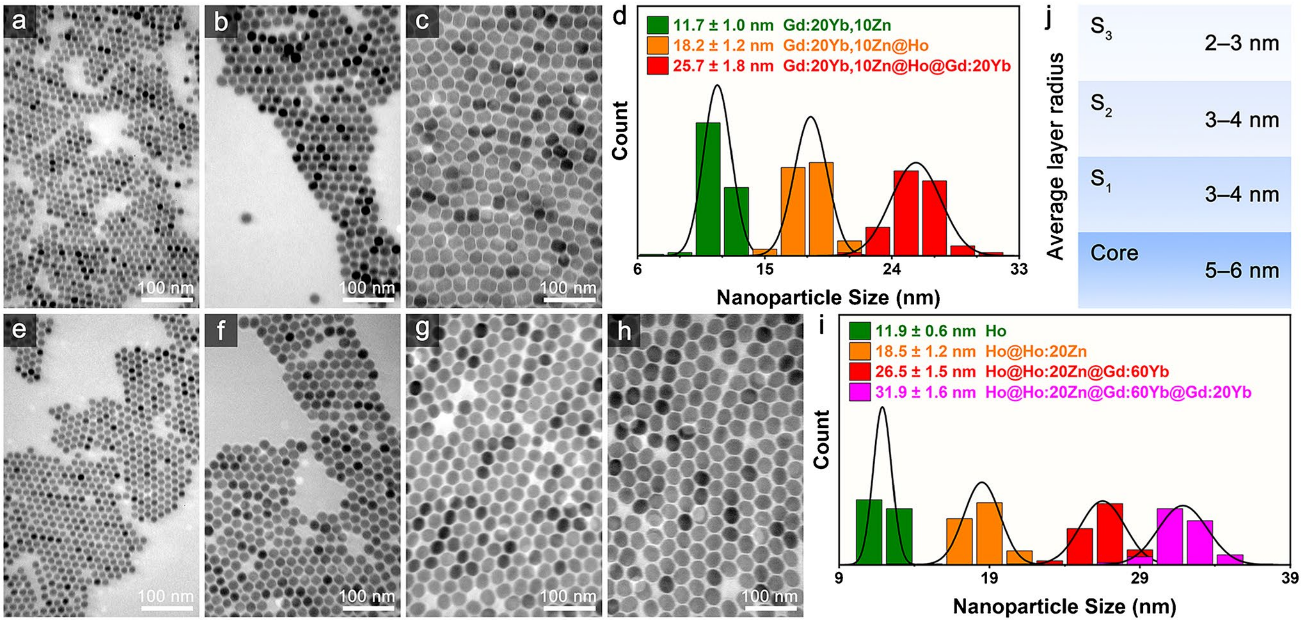

Fig. 1 (**a**)–(**d**) TEM images of NaGdF$_4$:20%Yb^{3+},10%Zn^{3+} (abbreviated as Gd:20Yb,10Zn, similarly hereinafter) core-only, Gd:20Yb,10Zn@Ho core–shell, Gd:20Yb,10Zn@Ho@Gd:20Yb core–double-shell UCNPs and respective size distribution diagram, respectively. (**e**)–(**i**) TEM images of Ho core-only, Ho@Ho:20Zn core–shell, Ho@Ho:20Zn@Gd:60Yb core–double-shell, Ho@Ho:20Zn@Gd:60Yb@Gd:20Yb core–triple-shell UCNPs and respective size distribution diagram, respectively. (**j**) Schematic illustration of average core radius and shell thicknesses for synthesized core–multi-shell UCNPs. S$_1$–S$_3$ stand for the first, second and third shell

Fig. 2 (**a**) Shifts of the selected (201) peak for different Yb@Ho@Ho UCNPs. (**b**) Schematic illustrations of lattice distortion and possible offset. (**c**) Shifts of the selected (201) peak for different Yb@Ho@Yb UCNPs. (**d**) Shifts of the selected (201) peak for different Ho@Ho@Yb@Yb UCNPs

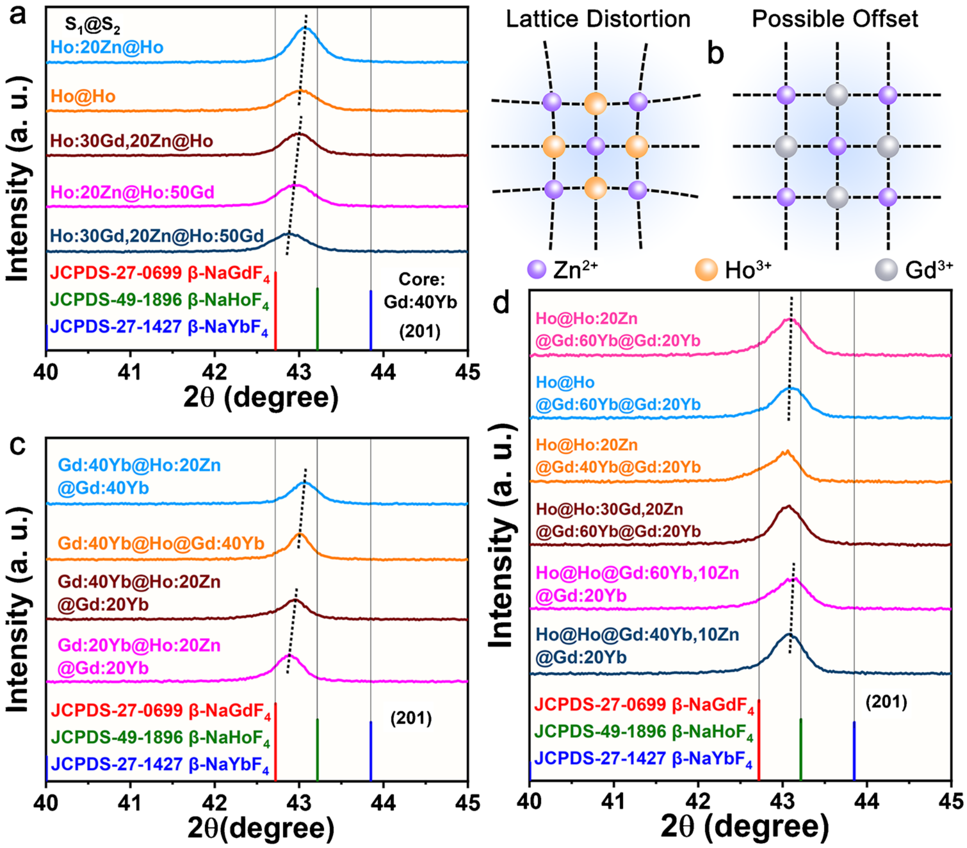

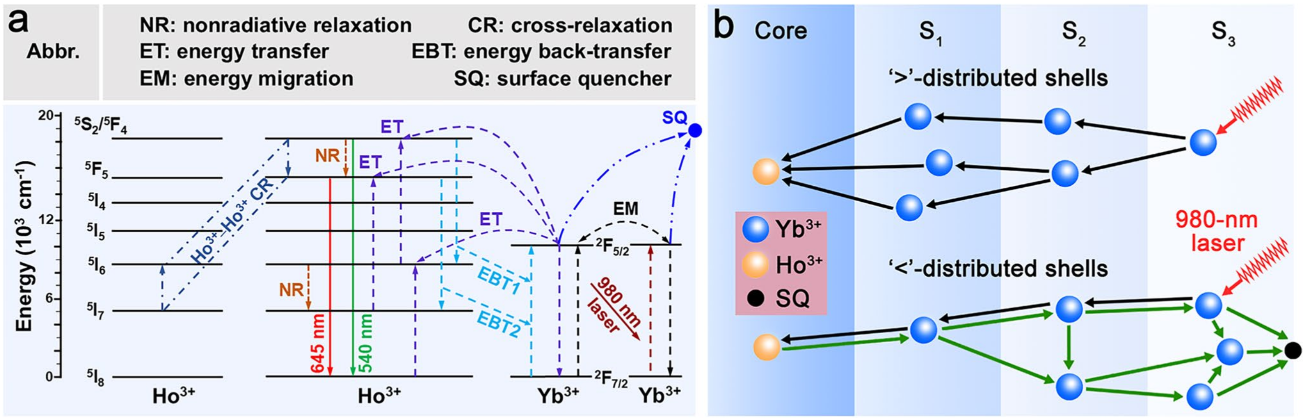

Fig. 3 (**a**) Energy diagrams and possible UCL-related mechanisms in the Yb^{3+}–Ho^{3+} system. (**b**) Schematic illustrations of energy mechanisms in Yb^{3+} '>' and '<'-distributed multi-shell structures. '>' and '<'-distributions stand for high-to-low and low-to-high gradients from inner to outer shells, respectively. S_1–S_3 stand for the first, second and third shell

previous works [46, 48]. In Fig. 2a, the degree sequence for $S_1@S_2$ is $NaHoF_4$:30%Gd^{3+},20%Zn^{2+}@$NaHoF_4$:50%Gd^{3+} (abbreviated as Ho:30Gd,20Zn@Ho:50Gd, similarly hereinafter) < Ho:20Zn@Ho:50Gd < Ho@Ho < Ho:20Zn@Ho, with very close result of Ho:30Gd,20Zn@Ho and Ho@Ho. Relevant ionic radius sequence being Gd^{3+} (1.1069 Å) > Ho^{3+} (1.0722 Å) > Yb^{3+} (1.0422 Å) > Zn^{2+} (0.9665 Å) under nine-coordination environment [49, 50], $S_1@S_2$ of Ho:20Zn@Ho got the highest angle. Since Ho:30Gd,20Zn@Ho:50Gd contained the largest Gd^{3+} quantity, its peak degree should be the lowest. Based on the average core and shell sizes calculated from TEM images, S_2 was larger in volume than S_1 (see Note 1 in SI), which means 20 mol% of S_1-located Zn^{2+} ions was difficult to offset the shift by 50 mol% of S_2-located Gd^{3+} ions, so Ho:20Zn@Ho:50Gd exhibited a lower angle than that of Ho@Ho. The comparable degree values of Ho:30Gd,20Zn@Ho and Ho@Ho implied that lattice distortion offset might occur in single layer (Fig. 2b).

In Fig. 2c, the degree sequence is Gd:40Yb@Ho@Gd:40Yb < Gd:40Yb@Ho:20Zn@Gd:40Yb, and Gd:20Yb@Ho:20Zn@Gd:20Yb < Gd:40Yb@Ho:20Zn@Gd:20Yb UCNPs, in accordance with the crystal radius sequence above. Note that for Gd:40Yb@Ho@Gd:40Yb and Gd:40Yb@Ho:20Zn@Gd:20Yb UCNPs, both at 20 mol%, substitution of Ho^{3+} with Zn^{2+} might induce larger lattice shrink in S_1 than substitution of Gd^{3+} with Yb^{3+} in S_2 did, but the volume of S_2 was larger than S_1. The eventual degrees were relatively comparable. In triple-shell structures (Fig. 2d), with more Gd^{3+} and Yb^{3+} ions in shells while the total Zn^{2+} content ratios were decreased by larger sample volumes, peak shifts became relatively indistinguishable.

Combined with peak shifts of other selected samples (Fig. S11, S14 and S15), it can be deduced that, for synthesized UCNPs, distinct ionic radii of content ions give rise to shifts of diffraction peaks following the Bragg's Law. Shifts can be partly offset in single layer, and weakened by more shell coatings with varied content.

Basic energy mechanisms for the Yb^{3+}–Ho^{3+} UCL system

In conventional $NaREF_4$ UCNPs, Yb^{3+} sensitizers and Ho^{3+} activators are usually co-doped in inert ($NaYF_4$, $NaGdF_4$ and $NaLuF_4$) or active ($NaYbF_4$) matrixes [51], and Ho-based UCL in the visible region mainly contains green and red emissions [52]. In a typical UCL process [53, 54], as shown in Fig. 3a, Yb^{3+} ions first capture 980-nm photons upon c. w. (continuous wave) or pulsed laser excitation, and conduct the $^2F_{7/2}$ (Yb^{3+}) → $^2F_{5/2}$ (Yb^{3+}) transition. Next, $^2F_{5/2}$-state Yb^{3+} ions sensitize Ho^{3+} ions onto the intermediate $^5I_6$ and green-emitting $^5S_2/^5F_4$ states via the energy transfer (ET) of $^2F_{5/2}$ (Yb^{3+}) + $^5I_8$ (Ho^{3+}) → $^2F_{7/2}$ (Yb^{3+}) + $^5I_6$ (Ho^{3+}) and sequentially $^2F_{5/2}$ (Yb^{3+}) + $^5I_6$ (Ho^{3+}) → $^2F_{7/2}$ (Yb^{3+}) + $^5S_2/^5F_4$ (Ho^{3+}) transitions, respectively. Finally, the green UCL peaked at ~ 541 nm is obtained via the $^5S_2/^5F_4$ (Ho^{3+}) → $^5I_8$ (Ho^{3+}) transition. To populate the red-emitting $^5F_4$ state, there happens cross-relaxation (CR) of the $^5F_4/^5S_2$ ($Ho_1{}^{3+}$) + $^5I_7$ ($Ho_2{}^{3+}$) → $^5F_5$ ($Ho_1{}^{3+}$) + $^5I_6$ ($Ho_2{}^{3+}$) transition, or non-radiative relaxation (NR) of the $^5F_4/^5S_2$ (Ho^{3+}) → $^5F_5$ (Ho^{3+}) transition, or firstly NR of the $^5I_6$ (Ho^{3+}) → $^5I_7$ (Ho^{3+}) then ET of the $^2F_{5/2}$ (Yb^{3+}) + $^5I_7$ (Ho^{3+}) → $^2F_{7/2}$ (Yb^{3+}) + $^5F_5$ (Ho^{3+}) transitions, after which the red UCL peaked at ~ 643 nm is obtained via the $^5F_5$ (Ho^{3+}) → $^5I_8$ (Ho^{3+}) transition. Normally, the green emission is much stronger than the red one [55].

In our Ho@Yb and Yb@Ho UCNPs, where Yb^{3+} sensitizers and Ho^{3+} activators are separated in different layers, ET is achieved by interfacial energy transfer (IET)[56]. Besides, energy migration (EM) of the $^2F_{5/2}$ ($Yb_1{}^{3+}$) + $^2F_{7/2}$

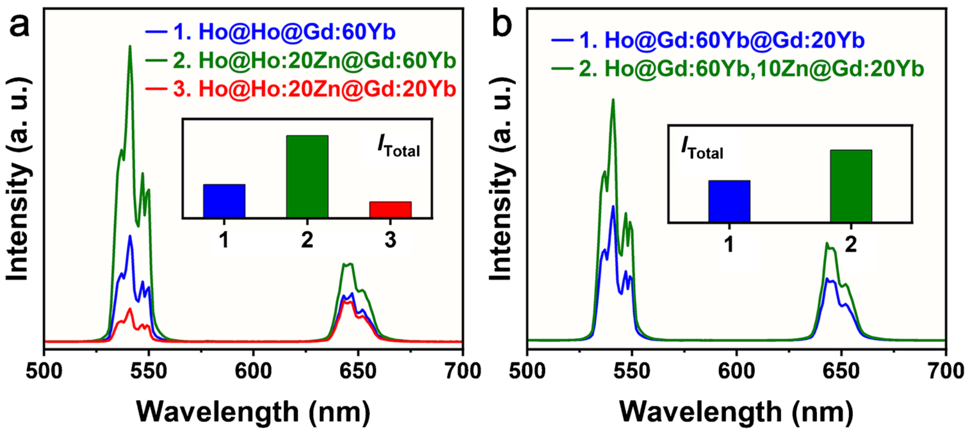

Fig. 4 (**a**) UCL spectra and I_{Total} of Ho@Ho@Gd:60Yb, Ho@Ho:20Zn@Gd:60Yb and Ho@Ho:20Zn@Gd:20Yb UCNPs. (**b**) UCL spectra and I_{Total} of Ho@Gd:60Yb@Gd:20Yb and Ho@Gd:60Yb,10Zn@Gd:20Yb UCNPs

(Yb$_2^{3+}$) → $^2F_{7/2}$ (Yb$_1^{3+}$) + $^2F_{5/2}$ (Yb$_2^{3+}$) transitions, and energy back-transfer (EBT) of the $^5F_4/^5S_2$ (Ho^{3+}) + $^2F_{7/2}$ (Yb^{3+}) → $^5I_6$ (Ho^{3+}) + $^2F_{5/2}$ (Yb^{3+}) and $^5F_5$ (Ho^{3+}) + $^2F_{7/2}$ (Yb^{3+}) → $^5I_7$ (Ho^{3+}) + $^2F_{5/2}$ (Yb^{3+}) transitions, can be easily initiated by highly doped Yb^{3+} and Ho^{3+} ions with close distances [42]. These processes can short-circuit the excitation energy to inner defects (IDs) and surface quenchers (SQs) via pathways such as EM–…–EM–ID, EBT–EM–SQ, and increase energy loss. With '>'-distributed (high-to-low gradient from inner to outer shells) Yb^{3+} concentrations in multi-shell structures [57], Gd:60Yb@Gd:40Yb@Gd:20Yb for example, negative influences from EBT and EM can be suppressed for enhanced sensitizing energy supply inwards (Fig. 3b).

Basic mechanisms of Zn^{2+}-induced UCL finetuning

Lattice manipulation by co-doping has been widely accepted and utilized as an effective chemical method for UCL finetuning [26]. With lattice shrink or expansion due to hetero-ion substitution and interstitial in the host matrix, the crystal field symmetry around Ho^{3+} and Yb^{3+} ions is lowered, promoting their 4f–4f transition abilities and thus increasing UCL intensities [27]. Generally, there is an optimal hetero-ion concentration for each nanoparticle structure. Too high doping levels can profoundly decrease UCL by superfluous lattice distortion [58], energy-quenching interstitial ions [29, 59], restoration of local symmetry [60], and more IDs [61]. Additionally, with non-trivalent hetero-ion dopants, to maintain charge balance, F$^-$ vacancies (V$_F^-$) form as IDs in the NaREF$_4$ matrix, which can also quench energy [31, 62].

Zn^{2+} was chosen as the hetero-ion. With X-ray photoelectron spectroscopy (XPS) characterization, the successful Zn^{2+} doping and the existence of V$_F^-$ can be validated [33, 63, 64] (see Fig. S17 and relevant analysis). Additionally, the Zn [2]$^+$-induced lattice distortion was further simulated via the Ho–F bond length (see Fig. S18 and relevant analysis), and the Fourier transform infrared spectra in Fig. S19 suggested that the condition of SQs should not be much influenced by Zn [2]$^+$ doping in different layers [65, 66]. Based on our previous work [48], to better compare and study the structural influences on lattice distortion, Zn^{2+} ions were separately co-doped with Ho^{3+} and Yb^{3+} ions by concentrations of 20 and 10 mol%, the generally positive effects of which were identified by simple experimental verification. As shown in Fig. 4, the total UCL intensity (I_{Total}) of Ho@Ho:20Zn@Gd:60Yb and Ho@Gd:60Yb,10Zn@Gd:20Yb UCNPs increased by 2.45 and 1.72 times compared with Ho@Ho@Gd:60Yb and Ho@Gd:60Yb@Gd:20Yb UCNPs, respectively. Apart from that, due to the fact that sensitization by 20 mol% of Yb^{3+} ions was insufficient for core@S$_1$ of Ho@Ho, I_{Total} of Ho@Ho:20Zn@Gd:20Yb UCNPs much weakened, illustrating the structural rationality of designed active shells such as the outmost Gd:60Yb and S$_1$@S$_2$ of Gd:60Yb@Gd:20Yb in this research.

Zn^{2+}-doped Yb@Ho@Ho structures

Given that surface energy quenching is a deciding factor of UCL intensity and lifetimes, we designed different NaGdF$_4$:40%Yb^{3+}@NaHoF$_4$:Gd^{3+}@NaHoF$_4$:Gd^{3+} (abbreviated as Gd:40Yb@Ho:Gd@Ho:Gd, or more simplified as Yb@Ho@Ho, similarly hereinafter) double-shell UCNPs to structurally avoid energy quenching pathways such as EBT–EM–SQ. As shown in Fig. 5a and Table S1, the 4f–4f transition ability of Ho^{3+} ions was raised with lattice distortion by Zn^{2+} hetero-ions doped in S$_1$ and S$_2$, but all samples emitted significantly weak I_{Total} compared with Ho@Ho@Gd:60Yb UCNPs. It has been well proved that, unlike the case for IET RE^{3+}–RE^{3+} transitions that decrease with inert shell separation [67], inert host matrixes hardly block the photon capture of Yb^{3+} sensitizers [68–71]. This means the sensitizing energy supply via Yb^{3+}–Ho^{3+} ET would be negligibly hindered with inert shell coatings even though the 980-nm excitation laser needed to penetrate both S$_1$ and S$_2$ before reaching the core-located Yb^{3+} ions. Accordingly, the

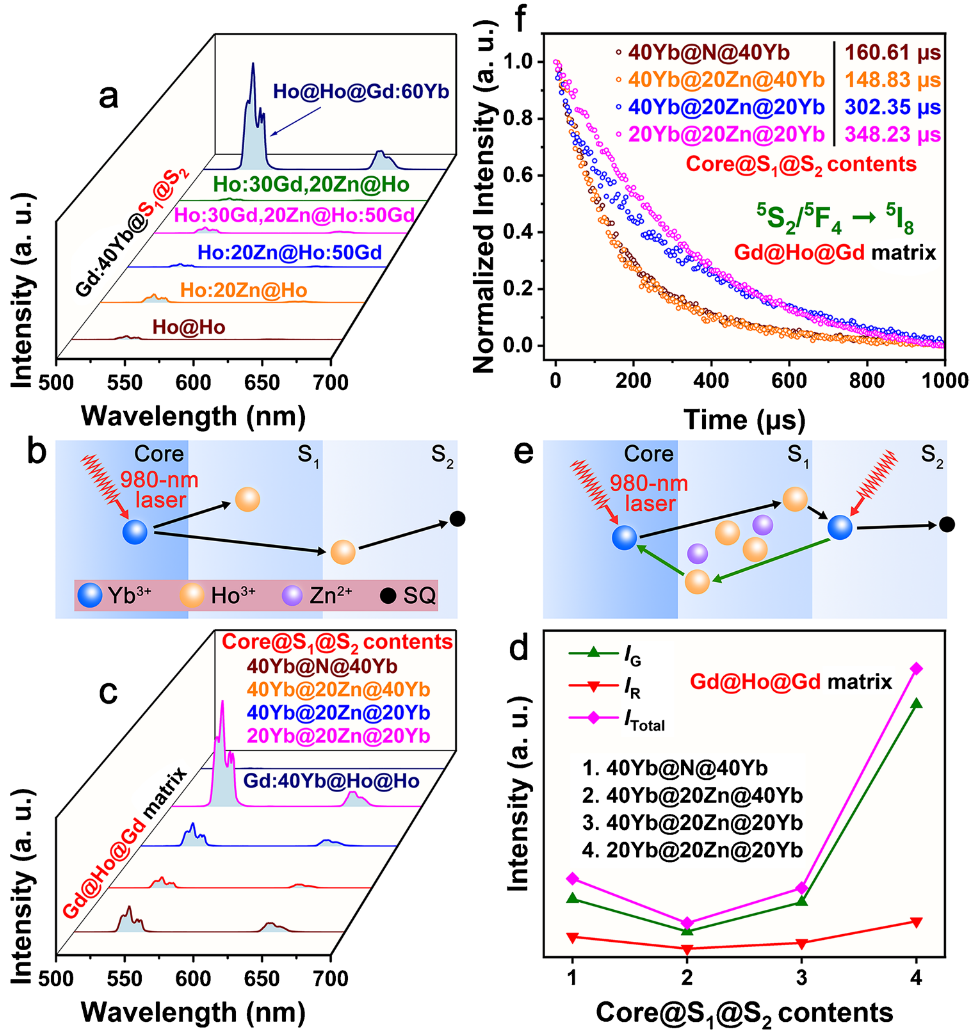

Fig. 5 (**a**) UCL spectra of Zn^{2+}-doped Yb@Ho@Ho UCNPs. Ho@Ho@Gd:60Yb sample is selected as reference. (**b**) Schematic illustrations of the ET–SQ pathway. (**c**) UCL spectra and (**d**) UCL property line chart of different Zn^{2+}-doped Yb@Ho@Yb UCNPs, respectively. Gd:40Yb@Ho@Ho sample is selected as reference. (**e**) Schematic illustrations of Yb^{3+}(core)–Ho^{3+}(S_1)–Yb^{3+}(S_2) and Yb^{3+}(S_2)–Ho^{3+}(S_1)–Yb^{3+}(core) pathways. (**f**) UCL decay curves and fitted lifetimes of UCNPs in (c). "N" in 40Yb@N@40Yb stands for "None". S_1 and S_2 stand for the first and second shells, respectively. I_G, I_R and I_{Total} stand for the green, red and total UCL intensity, respectively

possible reason for I_{Total} decrease were still surface energy quenching. S_2-located Ho^{3+} ions can readily interact with SQs and get depopulated from their excited states via the ET–SQ pathway (Fig. 5b). Compared with EBT–EM–SQ ones, the ET–SQ pathway can quench both the emissive $^5S_2$/$^5F_4$ and $^5F_5$, and intermediate $^5I_6$ and $^5I_7$ states, aggravating energy loss and restraining UCL. In brief, the Yb@Ho structures were not optimal due to severe energy quenching.

Zn^{2+}-doped Yb@Ho@Yb structures

Different Gd:Yb@Ho:Gd@Gd:Yb double-shell UCNPs with core- and S_1-doped Zn^{2+} ions were prepared and investigated. Compared to Gd:40Yb@Ho@Ho UCNPs, I_{Total} of Gd:40Yb@Ho@Gd:40Yb UCNPs drastically increased by 45.60 times (Fig. 5c, 5d and **Table S2**), indicating the much less surface energy quenching in S_1 than S_2. Interestingly, with 20 mol% of S_1-doped Zn^{2+} ions, I_{Total} decreased more than half. Since core- and S_2-located Yb^{3+} ions are highly doped and adjacent to S_1-located Ho^{3+} ions, negative energy pathways of Yb^{3+}(core)–Ho^{3+}(S_1)–Yb^{3+}(S_2) and Yb^{3+}(S_2)–Ho^{3+}(S_1)–Yb^{3+}(core) both formed (Fig. 5e), where S_1-located Ho^{3+} ions participated as assistant energy donors rather than final accepters. With promoted 4f–4f transitions by Zn^{2+} doping, the Ho^{3+}–Yb^{3+} EBT was exacerbated for more energy loss. Our analysis was evidenced by Gd:40Yb@Ho:20Zn@Gd:20Yb and Gd:20Yb@Ho:20Zn@Gd:20Yb UCNPs, where I_{Total} achieved 2.03 and much higher 8.49 times of enhancement, respectively, compared with Gd:40Yb@Ho:20Zn@Gd:40Yb UCNPs. Besides, more proof was provided by green-emission decay lifetimes (τ_G) with single-exponential fitting. As shown in Fig. 5f, τ_G decreased from 160.61 to 148.83 μs with S_1 of Ho:20Zn, and increased to 302.35 μs with S_2 of Gd:20Yb, and further increased to 348.23 μs with both core and S_2 of Gd:20Yb. Therefore, inward Ho^{3+}(S_1)–Yb^{3+}(core) EBT and outward Ho^{3+}(S_1)–Yb^{3+}(S_2) EBT simultaneously existed in Gd:40Yb@Ho:20Zn@Gd:40Yb UCNPs. Yb^{3+} concentration reduction in the core and S_2 can

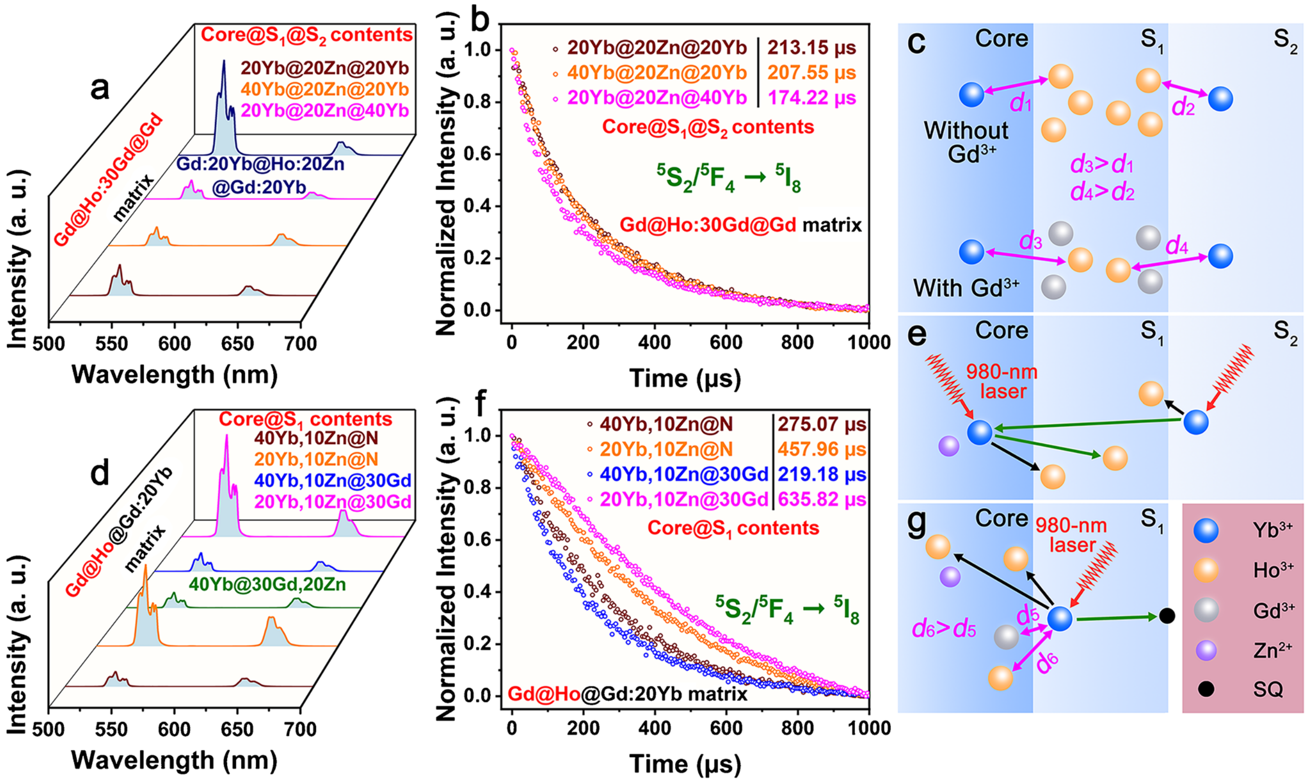

Fig. 6 (**a**) UCL spectra and (**b**) UCL decay curves and fitted lifetimes of Yb@Ho@Yb UCNPs with Zn^{2+} doping in S_1. Gd:20Yb@Ho:20Zn@Gd:20Yb sample is selected as reference. (**c**) Schematic illustrations of possible Yb^{3+}–Ho^{3+} ET distance variations by Gd^{3+} doping in S_1. (**d**) UCL spectra of Yb@Ho@Yb UCNPs with Zn^{2+} doping in the core. The Gd:40Yb@Ho:30Gd,20Zn@Gd:20Yb sample is selected as reference. (**e**) Schematic illustrations of positive Yb^{3+}(core)–Ho^{3+}(S_1), Yb^{3+}(S_2)–Ho^{3+}(S_1) and Yb^{3+}(S_2)–Yb^{3+}(core)–Ho^{3+}(S_1) pathways. (f) UCL decay curves and fitted lifetimes of UCNPs in (d). (g) Schematic illustrations of possible influences from surface quenching, Zn^{2+} doping and Gd^{3+} doping on Yb^{3+}–Ho^{3+} ET in Ho@Yb structures. "N" stands for "None". S_1 and S_2 stand for the first and second shells, respectively

effectively surpass the energy loss via EBT and enhance UCL properties.

With 30 mol% of S_1-located Gd^{3+} ions, UCL properties followed the variation regulations above. Gd:20Yb@Ho:30Gd,20Zn@Gd:20Yb UCNPs obtained the highest I_{Total} and τ_G values (Fig. 6a, 6b and Table S3), which were nevertheless noticeably lower compared with Gd:20Yb@Ho:20Zn@Gd:20Yb UCNPs. There were two possible explanations. First, as analyzed in Fig. 2b, the ionic radius sequence being Gd^{3+} (1.1069 Å) > Ho^{3+} (1.0722 Å) > Zn^{2+} (0.9665 Å), under high concentrations, the lattice expansion by substituting Ho^{3+} with larger Gd^{3+} ions might partly offset the lattice shrink by substituting Ho^{3+} with smaller Zn^{2+} ions, consequently weakening the enhancement of Ho^{3+} 4f–4f transitions by lattice distortion; Second, Gd^{3+} dopants reducing the Ho^{3+} quantity near the S_1/S_2 and core/S_1 interfaces by substitution, the overall Yb^{3+}–Ho^{3+} ET distance was indirectly lengthened (Fig. 6c). Considering the limited sensitizing efficiency from 20 mol% of Yb^{3+} ions, decreased quantity of Ho^{3+} ions finally got excited. More analysis would be offered afterwards.

For detailed insights, Zn^{2+} ions were co-doped with core-located Yb^{3+} ions in Gd:Yb@Ho:Gd@Gd:Yb double-shell UCNPs. As shown in Fig. 6d, S20 and Table S4, surprisingly, I_{Total} of Gd:40Yb,10Zn@Ho:30Gd@Gd:20Yb UCNPs did not dropped, and even got markedly enhanced by reducing Yb^{3+} concentration in the core (compared with the green line in Fig. 6d). These results suggested that promoted by lattice distortion, core-located 20 mol% of Yb^{3+} ions can be readily excited directly by 980-nm laser or indirectly by EM with S_2-doped Yb^{3+} ions, which sustained efficient sensitizing energy supply to S_1-located Ho^{3+} ions. Competitions between Yb^{3+}(S_2)–Yb^{3+}(core) EM and Yb^{3+}(S_2)–Ho^{3+}(S_1) ET may emerge, but can be alleviated by sequent Yb^{3+}(core)–Ho^{3+}(S_1) ET (Fig. 6e). Yb^{3+}(S_2)–Yb^{3+}(core) EM was also less detrimental than Yb^{3+}(core)–Yb^{3+}(S_2) EM in that excited Yb^{3+} ions were farther from SQs for reduced surface energy quenching. However, frequent Ho^{3+}(S_1)–Yb^{3+}(core) EBT remained in core of Gd:40Yb,10Zn, so 20 mol% of Yb^{3+} concentration cut into core of Gd:20Yb,10Zn led to I_{Total} enhancement of over 4 times as in Fig. S20. UCL lifetimes further proved the mechanism. τ_G prominently increased from 275.07 to 457.96, and from 219.18 to 635.82 μs after Yb^{3+} concentration reduction from core@S_1 of Gd:40Yb,10Zn@Ho to Gd:20Yb,10Zn@Ho, and from Gd:40Yb,10Zn@Ho:30Gd to Gd:20Yb,10Zn@Ho:30Gd, respectively (Fig. 6f). Such long lifetimes profited from the low Yb^{3+} sensitizer concentrations next to Ho^{3+} activators and highlighted structural optimization. Besides, the higher I_{Total} and τ_G values of Gd:20Yb,10Zn@Ho:30Gd@Gd:20Yb than Gd:20Yb,10Zn@Ho@Gd:20Yb UCNPs (Fig. S20) can be attributed to less CR-induced energy quenching, which would become a major factor after issues of sensitizing energy supply and surface quenching were dealt with. To conclude, Gd:20Yb,10Zn@Ho:30Gd@Gd:20Yb UCNPs optimized lattice distortion, ET, EBT, EM and CR mechanisms in Yb@Ho@Yb structures and possessed the best UCL performances.

Based on the above discussion, it can be conjectured that in Ho@Yb structures, Ho^{3+} ions competed with SQs for Yb^{3+} sensitizing energy (Fig. 6g), so Zn^{2+} co-doping with Ho^{3+} ions can increase the competitiveness of Ho^{3+} ions (Fig. 6g), especially those located farther from Yb^{3+} ions, and lengthening the overall Yb^{3+}–Ho^{3+} ET distance with Gd^{3+} co-doping functioned conversely (Fig. 6g). However, in Yb@Ho@Ho structures, core-located Yb^{3+} ions separated from SQs, the dependence of Yb^{3+}–Ho^{3+} ET on distance was relatively decreased, so S_1- and S_2-located Ho^{3+} ions can form strong competitions for ET, and most energy was quenched via the Yb^{3+}(core)–Ho^{3+}(S_2)–SQ pathway. In the Gd:40Yb@Ho:20Zn@Gd:40Yb structure with highly doped Yb^{3+} ions on both sides, under lattice distortion, Ho^{3+} ions near the S_1/S_2 interface via Yb^{3+}(core)–Ho^{3+}(S_1) ET can better compete with those near the core/S_1 interface for sensitizing energy from core Yb^{3+} ions. But then, excited Ho^{3+} ions near the S_1/S_2 interface got critically quenched by Ho^{3+}(S_1)–SQ or Ho^{3+}(S_1)–Yb^{3+}(S_2)–SQ pathways (Fig. 5e). The positive effects of core-located Yb^{3+} sensitization and Zn^{2+}-induced transition promotion were both undercut, so I_{Total} and τ_G fell. Similarly, Zn^{2+}-promoted Ho^{3+} ions near the core/S_1 interface via Yb^{3+}(S_2)–Ho^{3+}(S_1) ET can also better compete for sensitizing energy from S_2-located Yb^{3+} ions and then be quenched via inward Ho^{3+}(S_1)–Yb^{3+}(core) EBT (Fig. 5e). This meant overall more EBT and energy loss in Gd:40Yb@Ho:20Zn@Gd:40Yb structures. The structural influences on hetero-ion doping and UCL mechanisms can be clearly seen.

Zn^{2+}-doped Ho@Yb@Yb structures

The structural influences on lattice distortion were next examined in Ho@Gd:Yb@Gd:Yb structures. With a ‘ > ’-distributed (Fig. 3b) Yb^{3+} concentration, S_1@S_2 of Gd:60Yb@Gd:20Yb, Ho@Gd:60Yb@Gd:20Yb UCNPs displayed I_{Total} over a magnitude higher than that of Ho@Ho@Gd:60Yb UCNPs (Fig. 7a). With another 10 mol% of Zn^{2+} doping in S_1, I_{Total} value continued increasing by 72.46%, and further by 110.61% when S_1-located Yb^{3+} concentration reduced to 40 mol% (Fig. 7b and Table S5). However, additional Yb^{3+} concentration decrease into S_1 of Gd:20Yb,10Zn greatly cut down I_{Total} to a value even much lower than that of Ho@Gd:60Yb@Gd:20Yb UCNPs. These variations demonstrated that ‘ > ’-distributed S_1@S_2 of Gd:60Yb@Gd:20Yb can be modified, and S_1 of Gd:40Yb,10Zn gained relatively the best I_{Total} as the structure both maintained necessary sensitization efficiency with the aid of promoted Yb^{3+} 4f–4f transitions caused by lattice distortion, and partly decreased EBT frequency with acceptable Yb^{3+} concentration reduction.

τ_G values accorded with our analysis, increasing from 77.55 to 90.74 μs with S_1-doped Zn^{2+} ions, and then to 184.45 and 157.08 μs with sequent S_1-doped Yb^{3+} reduction (Fig. 7c). The lowest I_{Total} but second longest τ_G of Ho@Gd:20Yb,10Zn@Gd:20Yb UCNPs indicated that the UCL intensity is decided by both the quantity and non-radiative transition possibility of emissive-state Ho^{3+} ions. Short lifetimes denote severe energy loss typically via EBT, SQs and CR, as their reciprocals equal to the radiative and non-radiative transition rates that are the derivatives from respective transition possibility by time. Despite all this, if the quantity of $^5F_4$/$^5S_2$- and $^5F_5$-state Ho^{3+} ions is large enough to result in an increased number of $^5S_2$/$^5F_4 \rightarrow {}^5I_8$ and $^5F_5 \rightarrow {}^5I_8$ emissive transitions under conditions of severe energy loss, the UCL intensity would still rise. In other words, the outcome of a low possibility for a large candidate number, might be more than that of a high possibility for a small candidate number (Fig. 7d). Therefore, high UCL intensities matched with short lifetimes are not irrational, especially in highly doped structures with high concentrations of activators.

The above analysis also implied that UCL lifetimes sometimes might be determined by emissive-state Ho^{3+} quantities. The higher τ_G value of 348.23 μs for Gd:20Yb@Ho:20Zn@Gd:20Yb than 213.15 μs for Gd:20Yb@Ho:30Gd,20Zn@Gd:20Yb UCNPs was an example (Fig. 5f and 6b). Although undergoing relatively less Ho^{3+}(S_1)–Yb^{3+}(S_2) and Ho^{3+}(S_1)–Yb^{3+}(core) EBT due to Gd^{3+}-induced lengthening of overall Yb^{3+}–Ho^{3+} ET distance as analyzed, fewer Ho^{3+} ions in the latter structure got excited. The final non-radiative transition possibility for individual Ho^{3+} ion might still be higher and τ_G was lowered.

In Ho:Gd@Gd:Yb@Gd:Yb structures, with core of Ho:50Gd, ‘ > ’-distributed S_1@S_2 of Gd:60Yb,10Zn@Gd:20Yb exhibited the highest I_{Total} and τ_G values (Fig. 7e, 7f and Table S6), even higher than those of Ho@Gd:40Yb,10Zn@Gd:20Yb UCNPs, which manifested that 50 mol% of core-located inert Gd^{3+} ions can not only reduce energy quenching by CR, but also partly shield excited

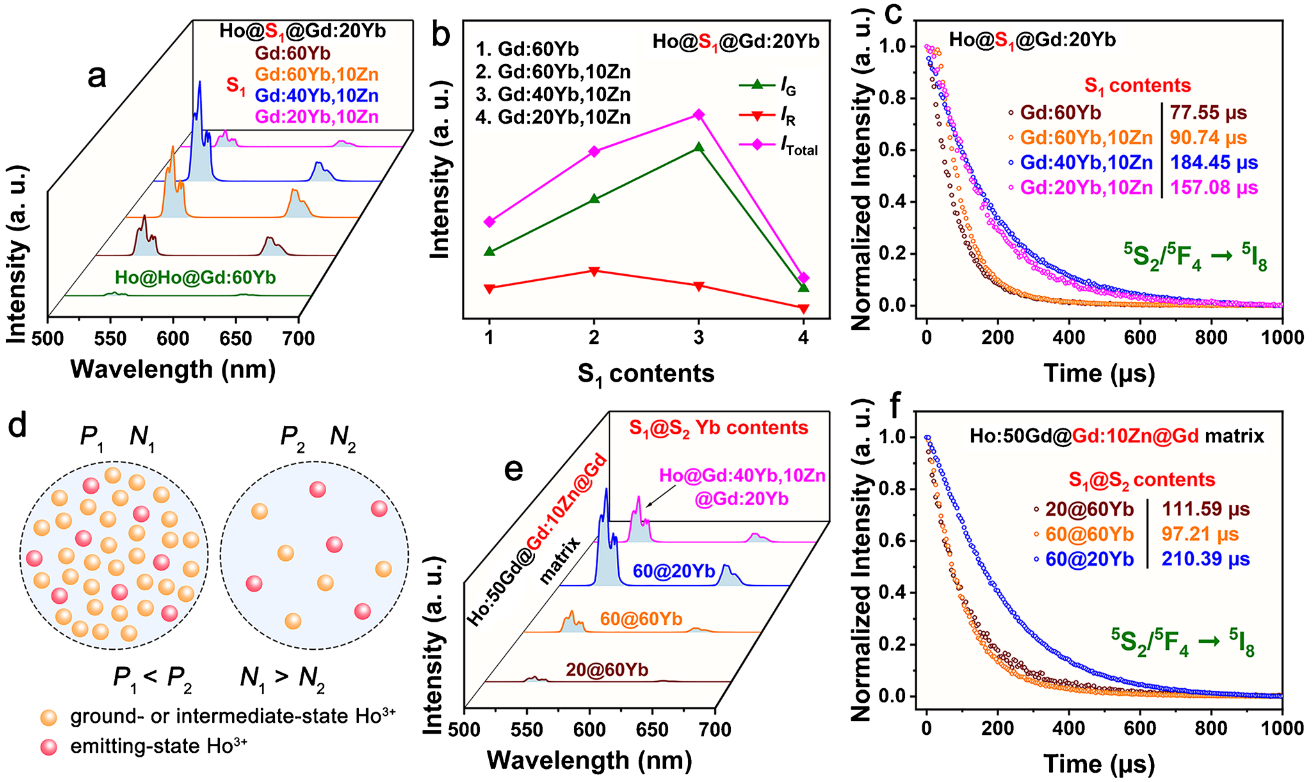

Fig. 7 (**a**) UCL spectra, (**b**) UCL property line chart and (**c**) decay curves and fitted lifetimes of Ho@Gd:Yb@Gd:Yb UCNPs with Zn^{2+} doping in S_1. Ho@Ho@Gd:20Yb sample is selected as reference. I_G, I_R and I_{Total} stand for the green, red and total UCL intensity, respectively. (**d**) Schematic illustrations of one possible example for high UCL intensities matched with short lifetimes. N_1 and N_2 refer to the quantities of emitting-state Ho^{3+} ions. P_1 and P_2 refer to the average possibilities of individual Ho^{3+} ion to be excited to emitting-state without non-radiative quenching. (**e**) UCL spectra and (**f**) decay curves and fitted lifetimes of Ho:50Gd@Gd:Yb@Gd:Yb UCNPs with Zn^{2+} doping in S_1. Ho@Gd:40Yb,10Zn@Gd:20Yb sample is selected as reference

Ho^{3+} ions from EBT. Besides, the '<'-distributed (low-to-high gradient from inner to outer shells, see Fig. 3b) Ho:50Gd@Gd:20Yb,10Zn@Gd:60Yb UCNPs possessed lower I_{Total} but higher τ_G values compared with Ho:50Gd@Gd:60Yb,10Zn@Gd:60Yb UCNPs. This phenomenon was consistent with our analysis for Yb@Ho@Yb structures that Gd:20Yb,10Zn can effectively decrease EBT. However, the ET efficiency was rather low in '<'-distributed structures, and hence lower I_{Total}. From another angle, the UCL properties of Ho:50Gd@Gd:20Yb,10Zn@Gd:60Yb UCNPs were also an example to prove that UCL intensity relies on both sensitizing energy supply and energy protection.

Zn^{2+}-doped Ho@Yb@Yb@Yb structures

Zn^{2+}-induced lattice distortion effects were studied in structures with a third active shell. As shown in Fig. 8a–8c and Table S7, although '>'-distributed Ho@Gd:60Yb@Gd:40Yb@Gd:20Yb UCNPs significantly increased I_{Total} and τ_G values compared with Ho@Gd:60Yb@Gd:20Yb UCNPs, additional Zn^{2+} dopants in triple-shell structures acquired only negative changes. Two possible reasons accounted for these results. First, EBT would be aggravated by promoted Yb^{3+} 4f–4f transitions upon S_1-doped Zn^{2+} ions. Second, to sustain charge balance, substitution of trivalent Gd^{3+} ions with bivalent Zn^{2+} hetero-ions produced V_F^- that can form IDs. These V_F^--induced IDs can partly add to crystal field asymmetry, and can cause energy loss at the same time either directly via quenching excited Ho^{3+} ions, or indirectly via pathways such as EBT–EM–ID (Fig. 8d). But in '>'-distributed triple active shells, where the sensitizing energy was not only well preserved and directed inwards but also reinforced by abundant Yb^{3+} quantities in shells, further promotion of Yb^{3+} 4f–4f transitions at the sacrifice of more V_F^--induced IDs as energy quenchers is unnecessary and should be avoided.

More proof and energy mechanism details can be derived from UCL alterations in Fig. 8a–8c. The relatively comparable I_{Total} and τ_G values between Ho@Gd:60Yb@Gd:40Yb@Gd:20Yb and Ho:50Gd@Gd:60Yb,10Zn@Gd:40Yb@Gd:20Yb UCNPs clearly revealed the Zn^{2+}-induced energy quenching, which was partly alleviated by Gd^{3+} shielding and compensated by reduced CR; The UCL properties of Ho@

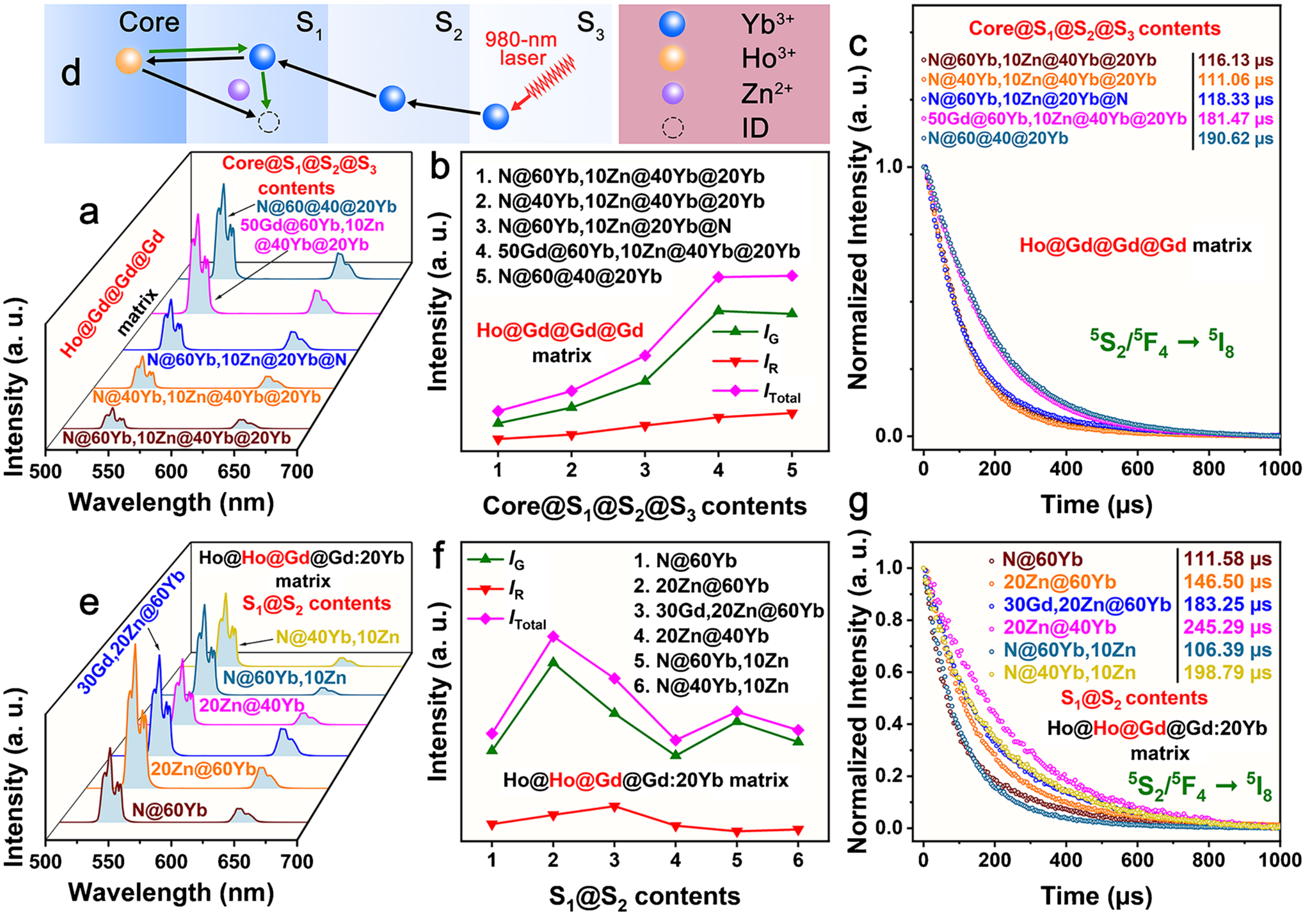

Fig. 8 (**a**) UCL spectra, (**b**) UCL property line chart and (**c**) decay curves and fitted lifetimes of Ho@Yb@Yb@Yb UCNPs with Zn^{2+} doping in S_1. (**d**) Schematic illustrations of possible energy quenching via EBT and V_F^--induced IDs in UCNPs with '>'-distributed triple active shells. (**e**) UCL spectra, (**f**) UCL property line chart and (**g**) decay curves and fitted lifetimes of Zn^{2+}-doped Ho@Ho@Yb@Yb UCNPs. "N" stands for "None". S_1–S_3 stand for the first, second and third shell. I_G, I_R and I_{Total} stand for the green, red and total UCL intensity, respectively

Gd:40Yb,10Zn@Gd:40Yb@Gd:20Yb UCNPs implied that Yb^{3+} reduction in S_1 can partly suppress EBT as discussed for Ho@Yb@Yb structures, but still cannot well solve the energy-quenching EBT–EM–ID pathways, and the '>'-distribution tendency was also weakened; As for the Ho@Gd:60Yb,10Zn@Gd:20Yb@Gd structure, its UCL properties showed that among these as-synthesized triple-shell UCNPs, energy loss via EBT and V_F^--induced IDs was heavier than via SQs. Moreover, the generally short lifetimes of Ho@Yb@Yb and Ho@Yb@Yb@Yb compared with Yb@Ho@Yb structures provided structural directions that double low-doped–active-shell adjacence is acceptable, and single highly-doped–active-shell adjacence brings about higher UCL intensities with lower lifetimes. To capture the essence, Zn^{2+} doping was not optimal in well-designed triple active shells with '>'-distributions mainly due to energy loss via V_F^--induced IDs.

Zn^{2+}-doped Ho@Ho@Yb@Yb structures

UCL properties of Ho@Ho@Gd:60Yb@Gd:20Yb triple-shell structures, with S_1- and S_2-doped Zn^{2+} hetero-ions, were measured and analyzed. As shown in Fig. 8e–8g and Table S8, I_{Total} increased by 1.90 and 1.51 times with S_1 of Ho:20Zn and Ho:30Gd,20Zn, respectively. As analyzed above for Yb@Ho@Yb structures (Fig. 6a and 6b), 30 mol% of Gd^{3+} dopants might partly offset Zn^{2+}-induced lattice distortion and meanwhile lengthen the overall Yb^{3+}–Ho^{3+} ET distance, so I_{Total} less enhanced. However, considering that the Yb^{3+} concentration in S_2 was as high as 60 mol% for easily triggered EBT, the overall increased distance between excited Ho^{3+} and ground-state Yb^{3+} ions, together with the energy shielding by inert Gd^{3+} ions, can partly reduce surface energy quenching via the EBT–EM–…–EM–ID pathways, as supported by higher τ_G values of 183.25 μs for S_1 of Ho:30Gd,20Zn than 146.57 and 111.58 μs for S_1 of Ho:20Zn and Ho, respectively.

$S_1@S_2$ of Ho@Gd:60Yb, Ho:20Zn@Gd:40Yb and Ho@Gd:40Yb,10Zn resulted in comparable I_{Total}, indicative of the idea of equivalent structures realized by Zn^{2+} doping. In our highly doped Ho@Yb and Yb@Ho structures, the quantity of sensitizers is far from enough while the quantity of activators is already much excessive. Under such conditions, for Yb^{3+}–Ho^{3+} ET processes, more adequate sensitization—either by more Yb^{3+} ions or by better 980-nm photon capture ability ascribed from Zn^{2+}-promoted Yb^{3+} 4f–4f transitions, and more emissive transitions—either by less energy loss or by Zn^{2+}-promoted Ho^{3+} 4f–4f transitions, can all raise the ET efficiency for higher I_{Total}. Accordingly, promoted Ho^{3+} or Yb^{3+} 4f–4f transitions paired with smaller Yb^{3+} quantities might acquire inapparently-changed I_{Total} values. The meaningful point lied in variations of other UCL parameters. As shown in Fig. 8g, τ_G values increased from 111.58 to 245.29 and 198.79 μs with $S_1@S_2$ of Ho@Gd:60Yb, Ho:20Zn@Gd:40Yb and Ho@Gd:40Yb,10Zn, respectively, since moderate Yb^{3+} concentration next to Ho^{3+} ions can effectively suppress EBT. Based on the enhanced UCL performances via Zn^{2+} co-doping with 20 mol% of Yb^{3+} ions in Fig. 6, the median τ_G and inapparently-changed I_{Total} values for $S_1@S_2$ of Ho@Gd:40Yb,10Zn (Fig. 8f) suggested that, Yb^{3+} being highly doped, Zn^{2+} ions co-doped with Ho^{3+} activators were more optimal than with Yb^{3+} sensitizers. After all, EBT was simultaneously exacerbated with promoted Yb^{3+} 4f–4f transitions. This regular pattern can be rechecked with the I_{Total} and τ_G sequences of $S_1@S_2$ of Ho@Gd:60Yb < Ho@Gd:60Yb,10Zn < Ho:20Zn@Gd:60Yb and Ho@Gd:60Yb,10Zn < Ho@Gd:60Yb < Ho:20Zn@Gd:60Yb, respectively (Fig. 8f and 8 g).

Besides, in Ho@Yb@Yb structures, $S_1@S_2$ of Gd:40Yb,10Zn@Gd:20Yb achieved higher I_{Total} than Gd:60Yb,10Zn@Gd:20Yb did (Fig. 7b), while in Ho@Ho@Yb@Yb structures, $S_2@S_3$ of same Gd:40Yb,10Zn@Gd:20Yb achieved the opposite outcome (Fig. 8f). Possible reasons were: First, Ho@Ho contained more Ho^{3+} ions and needed relatively more Yb^{3+} sensitizing for higher I_{Total}; Second, core@S_1 was larger than core and had smaller specific surface area, which meant that relatively fewer Yb^{3+} adjoined Ho^{3+} ions at the interface and the EBT frequency was partly reduced, so core@S_1 can better withstand Gd:60Yb,10Zn. As for UCL lifetimes, Gd:40Yb,10Zn had longer τ_G in both structures (Fig. 7c and 8g), further manifesting the non-positive correlation between UCL intensity and lifetimes as analyzed above in Fig. 7d. In fact, this non-positive correlation can be treated as a unique feature of highly doped UCNPs with different core–multi-shell structures.

To make a comprehensive conclusion, through Zn^{2+}-doped core–multi-shell structures, equivalence can be realized for I_{Total}, with designable τ_G. Zn^{2+} doping locations and specific core–multi-shell structures can both alter UCL regular patterns. Underlying UCL mechanisms are complex and deserve more in-depth exploration.

Application potentials of Zn^{2+}-doped core–multi-shell UCNPs

Our design of highly doped Ho^{3+} ions inside and high content ratio of Gd^{3+} ions in outer shells supported multi-channel bio-tracing including T_1-weighed MR, T_2-weighed magnetic resonance (MR), computed tomography (CT) and UCL imaging. For more demonstration, Ho@Ho:20Zn@Gd:60Yb@Gd:20Yb UCNPs was selected and dealt with PEI to be water-soluble. As shown in Fig. 9a–9c, even no more than 1.5 mg/mL, clear and distinguishable in vitro T_1-weighed MR, T_2-weighed MR and CT images, with signal intensities well following the concentration gradient (Table S9–S11 and Fig. S21), can be achieved within one sample. In vivo rat CT images also displayed relatively apparent variations in Hounsfield (HU) values from pre-injection of 88.7 to post-injection of 294.5 (Fig. 9d). These results underscored the great application potentials of our Zn^{2+}-finetuned UCNPs as multi-channel contrast agents for CT and MR imaging.

Assessing the potential application of nanomaterials requires a thorough examination of their biocompatibility and potential cytotoxicity (Fig. 9e)[72]. The cytotoxicity of UCNPs on TPC-1 human thyroid cancer cells and L929 fibroblasts was systematically evaluated using the CCK-8 assay. The UCNPs were dispersed in DMEM medium at varying concentrations (0.1, 0.2, 0.4, 0.8, 1.5 mg/mL) for co-culture with the respective cell types. The results showed that the UCNPs had negligible toxicity to both the cells across the range of tested concentrations (Fig. 9f). Moreover, the morphologic analyses of the UCNPs and the cells were conducted with scanning electron microscope (SEM). Figure 9g showed that, compared with the control group, the morphology and structure of cells exposed to UCNPs remained basically unchanged. These findings suggested the excellent in vitro biocompatibility and low toxicity of UCNPs, supporting their significant potential for clinical applications.

Fluorescence imaging experiments were conducted to verify the presence of luminescent properties of UCNPs in cells. Following co-culturing, cell nuclei were stained with DAPI (blue),

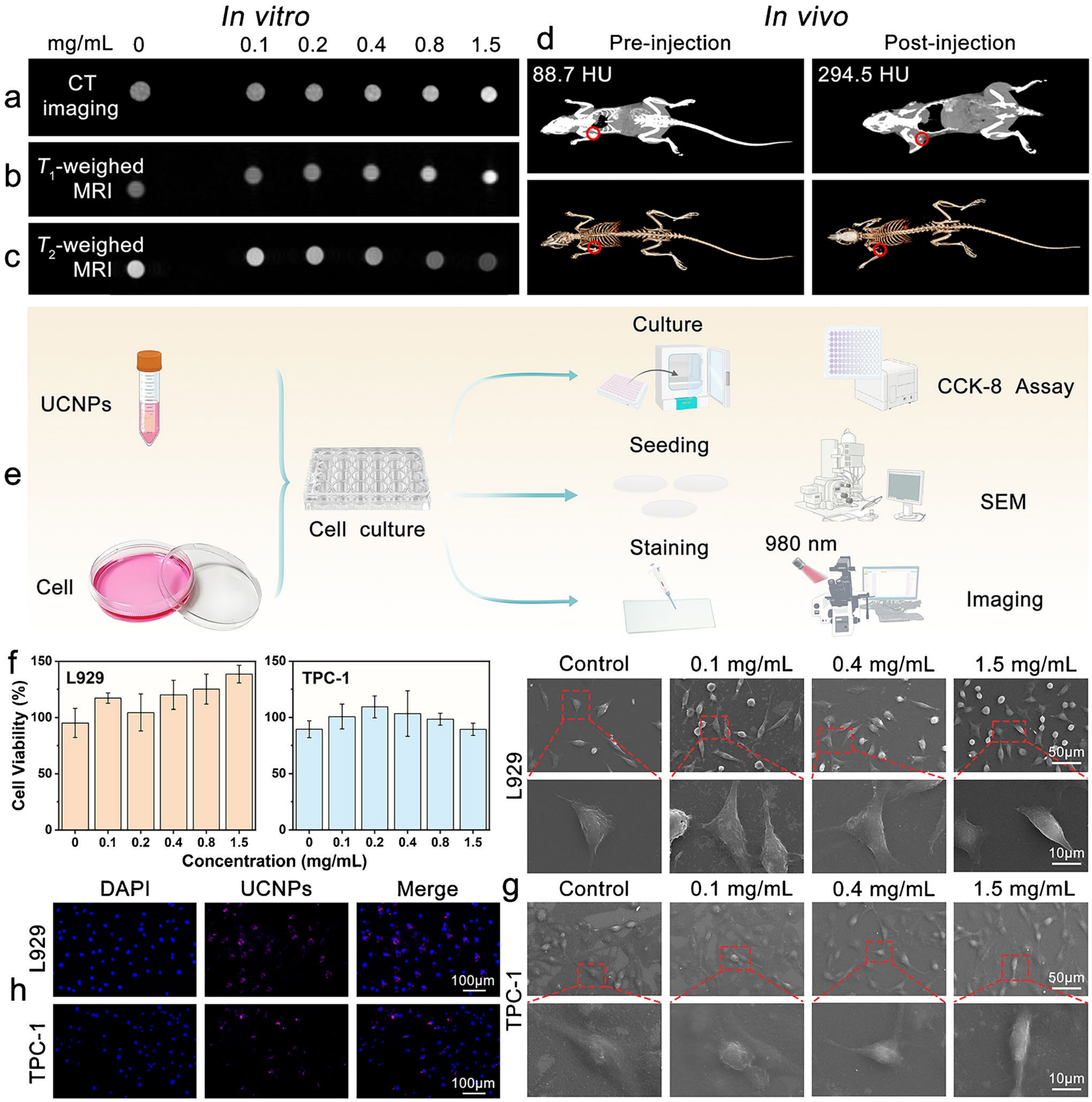

Fig. 9 (**a**)–(**c**) In vitro CT, T_1-weighed MR and T_2-weighed MR images of saline solutions with different concentrations of UCNPs, respectively. (**d**) In vivo CT images of the rat pre-injection and post-injection of UCNPs. (**e**) Schematic diagram of in vitro cell experiments. (**f**) Cell viability of L929 and TPC-1 cells at different concentrations of UCNPs (0, 0.1, 0.2, 0.4, 0.8, 1.5 mg/mL). (**g**) SEM images of cells co-cultured with UCNPs at three selected concentrations for 24 h. (**h**) Fluorescence images of L929 and TPC-1 cells after treatment with UCNPs

and their luminescent signals were visualized upon excitation with a 980 nm near-infrared laser. These results indicated that the UCL signals emitted by UCNPs in TPC-1 and L929 cells (Fig. 9h) were mainly concentrated around the cell nucleus, which aligned with those reported by Run Zhang et al [73]. The above results indicated that UCNPs not only emitted light in L929 cells, but also exhibited photophysical activity and UCL in the complex microenvironment of TPC-1 tumor cells.

In essence, UCNPs demonstrated outstanding in vitro biocompatibility, efficient cellular uptake, and sustained luminescence functionality post-endocytosis, thus strongly supporting their viability as probes for tumor imaging.

Conclusion

Through co-precipitation methods, series of core–multishell UCNPs highly doped with Yb^{3+} and Ho^{3+} ions were synthesized with rare earth chlorides and oleates, and the UCL was finetuned with Zn^{2+} dopants. The Yb@Ho@Ho structures had quite low UCL intensities due to surface energy quenching, while the Yb@Ho@Yb structures with core-doped Zn^{2+} ions and decreased Yb^{3+} concentration can alleviate EBT and surface quenching, and obtain lifetimes as high as 635.82 μs. In Ho@Yb@Yb, Ho@Yb@Yb@Yb and Ho@Ho@Yb@Yb structures, co-doping Zn^{2+} with Yb^{3+} or Ho^{3+} ions resulted in different UCL intensity and lifetime variations with layer numbers and Yb^{3+} distributions. Comparable UCL intensity with varied lifetimes ranging from 111.58 to 245.29 μs can be fulfilled with Zn^{2+} doping and different structures, and the optimal Zn^{2+}-doping strategy for one structure may not apply to another. It was found that by lattice distortion, Zn^{2+} doping promotes Yb^{3+} and Ho^{3+} 4f–4f transitions, but concomitant F^{-} vacancies can function as inner defects for energy quenching. Co-doping Gd^{3+} and Zn^{3+} in the $NaHoF_4$ matrix may cause offset of lattice distortion and lengthen the overall Yb^{3+}–Ho^{3+} ET distance for decreased UCL efficiency. Besides, due to the larger quantity of activators in highly-doped UCNPs, non-positive correlation between UCL intensity and lifetime may appear. Selected $NaHoF_4$@$NaHoF_4$@$NaGdF_4$:Yb^{3+}@$NaGdF_4$:Yb^{3+} UCNPs presented prominent multifunctional bio-application value in bio-imaging and as contrast agents for both CT and T_1/T_2-weigthed MR imaging. Our findings offer more theory insights and guidance for UCL finetuning with lattice distortion in highly doped and differently structured UCNPs, and better functionalize $NaHoF_4$-based nanomaterials from contrast agents to photo-induced diagnosis and treatments.

Supplementary Information The online version contains supplementary material available at https://doi.org/10.1007/s00604-025-07608-w.

Author Contributions Qiqi Ji: Experimental operation, Formal analysis, Data curation, Writing- original draft. Mengru Qin: Experimental operation, Formal analysis, Data curation, Writing- original draft. Tingting Zhu: Experimental operation, Data curation. Yanshuang Jiang: Experimental operation, Data curation. Yi Qu: Experimental operation, Data curation. Yufeng Wang: Experimental operation, Formal analysis, Data curation, Writing- original draft. Guangli Shi: Experimental operation, Resources, Software, Data curation. Chenghao Piao: Experimental operation, Software, Data curation, Resources, Funding acquisition. Ye Zhang: Experimental operation, Resources, Funding acquisition. Dongli Qi: Resources, Conceptualization, Formal analysis, Data curation, Project administration, Funding acquisition. Ye Kuang: Experimental operation, Formal analysis, Data curation, Resources, Conceptualization, Writing- original draft, Project administration, Funding acquisition, Writing-review & editing. Longhai Shen: Resources, Conceptualization, Project administration, Funding acquisition. Yiwei Wang: Experimental operation, Formal analysis, Data curation, Resources, Conceptualization, Project administration, Funding acquisition, Writing-review & editing.

Funding The work was financially supported by the National Natural Science Foundation of China (52502192, 12274304, 82073244), the fund of Department of Education of Liaoning Province (JYTQN2023046, JYTMS20230196), Team Construction Project of Liaoning Province Education Department (LJ222410164013), Liaoning Provincial Natural Science Foundation (Grant No.2024-MS-224), Scientific Research Project of Beijing Medical Reward Foundation (YXJL-2025–0483-0307).

Data availability The data of the manuscript are either included in the manuscript or supplementary materials.

Declarations

Clinical trial number Not applicable.

Competing interests The authors declare no competing interests.

References

1. Zhou Z, Wang X, Liao L (2024) Minimally invasive bladder stimulation via upconversion nanoparticle-mediated optogenetics. ACS Appl Nano Mater 7(5):5652–5660. https://doi.org/10.1021/acsanm.4c00704
2. Kim DW, Wrede P, Rodríguez-Camargo A, Chen Y, Dogan NO, Glück C, Lotsch BV, Razansky D, Sitti M (2025) Upconversion nanoparticle-covalent organic framework core–shell particles as therapeutic microrobots trackable with optoacoustic imaging. Adv Mater 2418425. https://doi.org/10.1002/adma.202418425
3. Liu D, Yan J, Wang K, Wang Y, Luo G (2022) Continuous synthesis of ultrasmall core-shell upconversion nanoparticles via a flow chemistry method. Nano Res 15(2):1199–1204. https://doi.org/10.1007/s12274-021-3625-3
4. Liu Y, Huang Y, Luo Y, Luo Y, Jiang L, Gallego-Ortega D, Cheng YY, Gale PA, Bao G (2025) Lanthanide-doped nanoprobes for microRNA detection. Coord Chem Rev 536:216644. https://doi.org/10.1016/j.ccr.2025.216644
5. Zeng J, Shang Y, Hao S, Chen T, Sun Z, Liu H, Yang C (2024) Advances in single upconverting nanoparticle sensing. Mater Today Phys 46:101520. https://doi.org/10.1016/j.mtphys.2024.101520
6. Cheng XW, Zhou J, Yue JY, Wei Y, Gao C, Xie XJ, Huang L (2022) Recent Development in Sensitizers for Lanthanide-Doped Upconversion Luminescence. Chem Rev 122(21):15998–16050. https://doi.org/10.1021/acs.chemrev.1c00772
7. Huang D, Li F, Ågren H, Chen G (2025) Inhibiting concentration quenching in Yb^{3+}-Tm^{3+} upconversion nanoparticles by suppressing back energy transfer. Nat Commun 16(1):4218. https://doi.org/10.1038/s41467-025-59452-4
8. Li C, Qu J, Li Y, Liu S, Tang Z, Wang Q, Ye J, Xu J, Niu N, Chen L et al (2025) Amino-tuned S-scheme ZIF nano-heterojunction coating up/downconversion nanoparticles for near-infrared-triggered catalytic therapy and bioimaging. Chem Eng J 508:160576. https://doi.org/10.1016/j.cej.2025.160576
9. Liu S, Yang S, Wang J, An Z, Wang J, Liao Y, Zhang Z, Tan J, Ye X, Zhou B (2025) Tunable tri-channel orthogonal full-color luminescence in nanostructure toward anticounterfeiting and information security. Laser Photonics Rev 19(8):2401652. https://doi.org/10.1002/lpor.202401652

10. Zheng J, Du P, An R, Liang Y, Wei Y, Liu S, Lei P, Zhang H (2025) Engineering tri-channel orthogonal luminescence in a single nanoparticle for information encryption. Inorg Chem Front 12(6):2506–2514. https://doi.org/10.1039/D4QI03199G
11. Wei H, Cai Z, Huang H, Wei G, Zhou B (2025) Ultra-sensitive low-temperature upconversion via interfacial energy transfer toward visual cryogenic nanothermometry. Adv Funct Mater e10764. https://doi.org/10.1002/adfm.202510764
12. Chen J, Liu C, Xi S, Tan S, He Q, Liang L, Liu X (2025) Optical nonlinearities in excess of 500 through sublattice reconstruction. Nature 643(8072):669–674. https://doi.org/10.1038/s41586-025-09164-y
13. Zhao J, Jin D, Schartner EP, Lu Y, Liu Y, Zvyagin AV, Zhang L, Dawes JM, Xi P, Piper JA et al (2013) Single-nanocrystal sensitivity achieved by enhanced upconversion luminescence. Nat Nanotechnol 8(10):729–734. https://doi.org/10.1038/nnano.2013.171
14. Wang Z, Meijerink A (2018) Concentration quenching in upconversion nanocrystals. J Phys Chem C 122(45):26298–26306. https://doi.org/10.1021/acs.jpcc.8b09371
15. Gao W, Zhang J, Ding P, Zhang C, Yan X, Han Q, Dong J (2024) Enhanced red UC emission of Er^{3+} ions by constructing multi-heterojunction core-shell nanoparticles. J Alloys Compd 1009:176893. https://doi.org/10.1016/j.jallcom.2024.176893
16. Yang X, Song R, Gong X, Deng H, He C, Liu J, Zhou P, Fu H (2024) Multi-shell structured nanomaterials with strong red upconversion emission for trimodal biomedical imaging. Ceram Int 50(1, Part B):1601–1606. https://doi.org/10.1016/j.ceramint.2023.10.253
17. Ren F, Wang F, Baghdasaryan A, Li Y, Liu H, Hsu R, Wang C, Li J, Zhong Y, Salazar F et al (2024) Shortwave-infrared-light-emitting probes for the in vivo tracking of cancer vaccines and the elicited immune responses. Nat Biomed Eng 8(6):726–739. https://doi.org/10.1038/s41551-023-01083-5
18. Zhu X, Liu X, Zhang H, Zhao M, Pei P, Chen Y, Yang Y, Lu L, Yu P, Sun C et al (2021) High-fidelity NIR-II multiplexed lifetime bioimaging with bright double interfaced lanthanide nanoparticles. Angew Chem Int Ed 60(44):23545–23551. https://doi.org/10.1002/anie.202108124
19. Wang J, Deng R, MacDonald MA, Chen B, Yuan J, Wang F, Chi D, Andy Hor TS, Zhang P, Liu G et al (2014) Enhancing multiphoton upconversion through energy clustering at sublattice level. Nat Mater 13(2):157–162. https://doi.org/10.1038/nmat3804
20. Zheng X, Kankala RK, Liu C-G, Wen Y, Wang S-B, Chen A-Z, Zhang Y (2022) Tailoring lanthanide upconversion luminescence through material designs and regulation strategies. Adv Opt Mater 10(12):2200167. https://doi.org/10.1002/adom.202200167
21. Johnson NJJ, He S, Diao S, Chan EM, Dai H, Almutairi A (2017) Direct evidence for coupled surface and concentration quenching dynamics in lanthanide-doped nanocrystals. J Am Chem Soc 139(8):3275–3282. https://doi.org/10.1021/jacs.7b00223
22. Cai Y, Lu M, Qin X, Jin D, Zhou J (2025) Understanding shell coating effects to overcome quenching in single anisotropic upconversion nanoparticles. Nat Commun 16(1):4927. https://doi.org/10.1038/s41467-025-60347-7
23. Wang J, Niu H, Chen H, Yuan S, Zheng S, Zhao T, Wu Y, Liu J, Che H, Zhang Y et al (2025) Achieving precision phototherapy from start to finish: integrating endosomal escape, respiration inhibition, and ROS release in a single upconversion nanoparticle. Small Methods 9(5):2401742. https://doi.org/10.1002/smtd.202401742
24. Gargas DJ, Chan EM, Ostrowski AD, Aloni S, Altoe MVP, Barnard ES, Sanii B, Urban JJ, Milliron DJ, Cohen BE et al (2014) Engineering bright sub-10-nm upconverting nanocrystals for single-molecule imaging. Nat Nanotechnol 9(4):300–305. https://doi.org/10.1038/nnano.2014.29
25. Wen S, Zhou J, Zheng K, Bednarkiewicz A, Liu X, Jin D (2018) Advances in highly doped upconversion nanoparticles. Nat Commun 9(1):2415. https://doi.org/10.1038/s41467-018-04813-5
26. Dong H, Sun L-D, Yan C-H (2021) Local structure engineering in lanthanide-doped nanocrystals for tunable upconversion emissions. J Am Chem Soc 143(49):20546–20561. https://doi.org/10.1021/jacs.1c10425
27. Mohanty S, Kaczmarek AM (2022) Unravelling the benefits of transition-metal-co-doping in lanthanide upconversion nanoparticles. Chem Soc Rev 51(16):6893–6908. https://doi.org/10.1039/D2CS00495J
28. Pandey P, Kaushik SD, Rajput P, Singh MN, Sharma RK, Giri S (2025) Nature of local disorder in β-$NaYF_4$-based, near-infrared upconverting core nanocrystals due to deliberate incorporation of a symmetry perturbing agent. Nanoscale 17(4):2269–2280. https://doi.org/10.1039/D4NR03951C
29. Zhao C, Kong X, Liu X, Tu L, Wu F, Zhang Y, Liu K, Zeng Q, Zhang H (2013) Li^+ ion doping: an approach for improving the crystallinity and upconversion emissions of $NaYF_4$:Yb^{3+}, Tm^{3+} nanoparticles. Nanoscale 5(17):8084–8089. https://doi.org/10.1039/C3NR01916K
30. Wang R, Song R, Wang C, Luo T, Hu J, Fu H (2024) Upconversion luminescence and temperature sensing performance of Zn^{2+}-doped Ba_2GdAlO_5: Yb^{3+}, Er^{3+} phosphors. Ceram Int 50(12):21083–21091. https://doi.org/10.1016/j.ceramint.2024.03.217
31. Cong T, Ding Y, Liu J, Zhao H, Hong X (2016) Synthesis and optical properties of Zn^{2+} doped $NaYF_4$: Yb^{3+}, Er^{3+} upconversion nanoparticles. Mater Lett 165:59–62. https://doi.org/10.1016/j.matlet.2015.11.109
32. Lu G, Zhang Y, Song J, Jing Y, Li X, Qin R, Zhai DB, Jiang J, Wang Y, Wang H (2025) Enhanced red upconversion luminescence in Fe^{3+}-activated $NaYF_4$: Yb, Er nanocrystals for rapid latent fingerprint recognition. J Lumin 282:121218. https://doi.org/10.1016/j.jlumin.2025.121218
33. Yamini S, Gunaseelan M, Kumar GA, Dannangoda GC, Martirosyan KS, Roy B, Senthilselvan J (2022) Tailoring the upconversion emission and magnetic properties of $NaGdF_4$:Yb, Er by Mg^{2+} or Fe^{3+} doping and optical trapping of individual magnetic nanoparticle at NIR 980 nm. Ceram Int 48(16):24003–24011. https://doi.org/10.1016/j.ceramint.2022.05.076
34. Verma P, Sarkar D, Rajput P, Singh MN, Sharma R, Giri S (2020) Synchrotron-based X-ray analysis: relating compressive lattice strain with the photoluminescence intensity of Li^+-doped β-$NaYF_4$:Yb^{3+}/Ln^{3+} ($Ln^{3+} = Ho^{3+}/Er^{3+}/Tm^{3+}$) upconversion crystals. Cryst Growth Des 20(1):468–478. https://doi.org/10.1021/acs.cgd.9b01426
35. Liu M, Shi Z, Wang X, Zhang Y, Mo X, Jiang R, Liu Z, Fan L, Ma C-G, Shi F (2018) Simultaneous enhancement of red upconversion luminescence and CT contrast of $NaGdF_4$:Yb,Er nanoparticles via L^{u3}+ doping. Nanoscale 10(43):20279–20288. https://doi.org/10.1039/C8NR06968A
36. Senthamarai R, Zhao Z, Liu C, Wang L, Zhang J (2025) Recent advances in lanthanide-doped upconversion nanoparticles for optical anticounterfeiting: challenges and opportunities toward practical implementation. Coord Chem Rev 542:216892. https://doi.org/10.1016/j.ccr.2025.216892
37. Kaur K, Kaur N, Swami K, Abhijith TS, Moun N, Kumar P, Khatri M, Shanmugam V (2025) Upconversion enabled innovation: transfer of lab sensor to smartphone based field device. Food Res Int 213:116547. https://doi.org/10.1016/j.foodres.2025.116547
38. Li B, Pan J, Zhang R, Han B, Zhao Y, Liu G, Tong Y, He Y, Xie G, Liu R et al (2025) Vascular magnifier for ultrahigh-resolution

visualization of cerebral vessels in vivo. Biomaterials 322:123356. https://doi.org/10.1016/j.biomaterials.2025.123356

39. Gómez-González E, Caro C, Martínez-Gutiérrez D, García-Martín ML, Ocaña M, Becerro AI (2021) Holmium phosphate nanoparticles as negative contrast agents for high-field magnetic resonance imaging: synthesis, magnetic relaxivity study and in vivo evaluation. J Colloid Interface Sci 587:131–140. https://doi.org/10.1016/j.jcis.2020.11.119
40. Zhang X, Blasiak B, Marenco AJ, Trudel S, Tomanek B, van Veggel FCJM (2016) Design and regulation of $NaHoF_4$ and $NaDyF_4$ nanoparticles for high-field magnetic resonance imaging. Chem Mater 28(9):3060–3072. https://doi.org/10.1021/acs.chemmater.6b00264
41. Ni D, Zhang J, Bu W, Zhang C, Yao Z, Xing H, Wang J, Duan F, Liu Y, Fan W et al (2016) PEGylated NaHoF4 nanoparticles as contrast agents for both X-ray computed tomography and ultra-high field magnetic resonance imaging. Biomaterials 76:218–225. https://doi.org/10.1016/j.biomaterials.2015.10.063
42. Kuang Y, Xu J, Wang C, Li T, Gai S, He F, Yang P, Lin J (2019) Fine-tuning Ho-based red-upconversion luminescence by altering $NaHoF_4$ core size and $NaYbF_4$ shell thickness. Chem Mater 31(19):7898–7909. https://doi.org/10.1021/acs.chemmater.9b01944
43. Lin H, Cheng Z, Xu D, Zheng X, Ge J, Xu L, Ma Y, Yang S, Zhang Y (2021) Constructing a small core–multishell nanostructure for Ho-based red upconversion emission. J Mater Chem C 9(12):4385–4392. https://doi.org/10.1039/D1TC00115A
44. Huang R, Liu S, Huang J, Liu H, Hu Z, Tao L, Zhou B (2021) Tunable upconversion of holmium sublattice through interfacial energy transfer for anti-counterfeiting. Nanoscale 13(9):4812–4820. https://doi.org/10.1039/D0NR09068A
45. Kuang Y, Xu J, Shi G, Hu T, Wang X, Li B, Liang Y, Qin P, Zeng W, Wang H et al (2025) Influence of Ho^{3+} and Yb^{3+} concentration distributions on Ce^{3+}-fine-tuned upconversion luminescence in highly doped core–multi-shell upconversion nanoparticles. J Alloys Compd 1036:181927. https://doi.org/10.1016/j.jallcom.2025.181927
46. Xu J, Wang B, Shi G, Hu T, Yang P, Kuang Y, Shen L (2024) Exploring energy mechanisms involved in the luminescence reduction due to Ce^{3+} doping via core-multishell upconversion nanoparticles highly doped with Ho^{3+} and Yb^{3+}. Ceram Int 50(10):17593–17603. https://doi.org/10.1016/j.ceramint.2024.02.248
47. Liu X, Deng R, Zhang Y, Wang Y, Chang H, Huang L, Liu X (2015) Probing the nature of upconversion nanocrystals: instrumentation matters. Chem Soc Rev 44(6):1479–1508. https://doi.org/10.1039/C4CS00356J
48. Kuang Y, Yang D, Gai S, He F, An B, Yang P (2023) Uncovering different responses and energy mechanisms of sensitizer and activator in host manipulation for upconversion nanoparticles. Inorg Chem 62(27):10805–10821. https://doi.org/10.1021/acs.inorgchem.3c01423
49. Baloch AAB, Alqahtani SM, Mumtaz F, Muqaibel AH, Rashkeev SN, Alharbi FH (2021) Extending Shannon's ionic radii database using machine learning. Phys Rev Mater 5(4):043804. https://doi.org/10.1103/PhysRevMaterials.5.043804
50. Alsalman M, Alghofaili YA, Baloch AAB, Alsadah H, Alsaui AA, Alqahtani SM, Muqaibel AH, Alharbi FH (2023) Outliers in Shannon's effective ionic radii table and the table extension by machine learning. Comput Mater Sci 228:112350. https://doi.org/10.1016/j.commatsci.2023.112350
51. Geng S, Li H, Lv Z, Zhai Y, Tian B, Luo Y, Zhou Y, Han S-T (2025) Challenges and opportunities of upconversion nanoparticles for emerging nir optoelectronic devices. Adv Mater 2419678. https://doi.org/10.1002/adma.202419678
52. Haase M, Schäfer H (2011) Upconverting nanoparticles. Angew Chem Int Ed 50(26):5808–5829. https://doi.org/10.1002/anie.201005159
53. Zhou J, Liu Q, Feng W, Sun Y, Li F (2015) Upconversion luminescent materials: advances and applications. Chem Rev 115(1):395–465. https://doi.org/10.1021/cr400478f
54. Vinícius-Araújo M, Shrivastava N, Silva Loures G, Krause RF, Sousa MH, de Santana RC, Bakuzis AF (2024) Integration of 3D fluorescence imaging and luminescent thermometry with core-shell engineered $NaYF_4$:Nd^{3+}/Yb^{3+}/Ho^{3+} nanoparticles. Inorg Chem 63(4):1840–1852. https://doi.org/10.1021/acs.inorgchem.3c03410
55. Gai S, Li C, Yang P, Lin J (2014) Recent progress in Rare Earth micro/nanocrystals: soft chemical synthesis, luminescent properties, and biomedical applications. Chem Rev 114(4):2343–2389. https://doi.org/10.1021/cr4001594
56. Zhou B, Li Q, Yan L, Zhang Q (2020) Controlling upconversion through interfacial energy transfer (IET): fundamentals and applications. J Rare Earths 38(5):474–482. https://doi.org/10.1016/j.jre.2020.01.009
57. Zhong Y, Rostami I, Wang Z, Dai H, Hu Z (2015) Energy migration engineering of bright rare-earth upconversion nanoparticles for excitation by light-emitting diodes. Adv Mater 27(41):6418–6422. https://doi.org/10.1002/adma.201502272
58. Yin D, Wang C, Ouyang J, Song K, Liu B, Cao X, Zhang L, Han Y, Long X, Wu M (2014) Enhancing upconversion luminescence of $NaYF_4$:Yb/Er nanocrystals by Mo^{3+} doping and their application in bioimaging. Dalton Trans 43(31):12037–12043. https://doi.org/10.1039/C4DT00172A
59. Cheng S, Cheng D, Su X, Zeng Y, Nie G, Zhan S, Wu X (2023) Manipulation phonon energy for improved thermometric sensitivity of only-core nanoparticles. J Alloys Compd 969:172367. https://doi.org/10.1016/j.jallcom.2023.172367
60. Wu K, Xi Z, Qiu R, Zhang J, Li Z (2024) Luminescence performance, temperature sensing characteristics and Judd-Ofelt theory analysis of Y_2MoO_6:Er^{3+}/Yb^{3+}/Li^+ upconversion phosphors. Ceram Int 50(24, Part B):53888–53898. https://doi.org/10.1016/j.ceramint.2024.10.241
61. Ding Y, Li Z (2022) Tuning the photoluminescence properties of β-$NaYF_4$:Yb,Er by B^{i3}+ doping strategy. Cryst Res Technol 57(4):2100162. https://doi.org/10.1002/crat.202100162
62. Lei L, Chen D, Xu J, Zhang R, Wang Y (2014) Highly intensified upconversion luminescence of Ca^{2+}-doped Yb/Er:$NaGdF_4$ nanocrystals prepared by a solvothermal route. Chem - Asian J 9(3):728–733. https://doi.org/10.1002/asia.201301514
63. Ye K, Li K, Lu Y, Guo Z, Ni N, Liu H, Huang Y, Ji H, Wang P (2019) An overview of advanced methods for the characterization of oxygen vacancies in materials. Trends Anal Chem 116:102–108. https://doi.org/10.1016/j.trac.2019.05.002
64. Ramasamy P, Chandra P, Rhee SW, Kim J (2013) Enhanced upconversion luminescence in $NaGdF_4$:Yb,Er nanocrystals by F^{e3}+ doping and their application in bioimaging. Nanoscale 5(18):8711–8717. https://doi.org/10.1039/C3NR01608K
65. Wang F, Wang J, Liu X (2010) Direct evidence of a surface quenching effect on size-dependent luminescence of upconversion nanoparticles. Angew Chem Int Ed 49(41):7456–7460. https://doi.org/10.1002/anie.201003959
66. Fan T, Zhang Q, Jiang Z (2011) Enhancement of the 1.5 µm emission in Y_2O_3:Er^{3+} nanocrystals by codoping with Li^+ ions. J Opt 13(1):015001. https://doi.org/10.1088/2040-8978/13/1/015001
67. Su Q, Han S, Xie X, Zhu H, Chen H, Chen C-K, Liu R-S, Chen X, Wang F, Liu X (2012) The effect of surface coating on energy migration-mediated upconversion. J Am Chem Soc 134(51):20849–20857. https://doi.org/10.1021/ja3111048

68. Qian LP, Yuan D, Yi GS, Chow Moog G (2009) Critical shell thickness and emission enhancement of $NaYF_4$:Yb,Er/NaY$_F$4/silica core/shell/shell nanoparticles. J Mater Res 24(12):3559–3568. https://doi.org/10.1557/jmr.2009.0432
69. Johnson NJJ, Korinek A, Dong C, van Veggel FCJM (2012) Self-focusing by Ostwald ripening: a strategy for layer-by-layer epitaxial growth on upconverting nanocrystals. J Am Chem Soc 134(27):11068–11071. https://doi.org/10.1021/ja302717u
70. Zhang F, Che R, Li X, Yao C, Yang J, Shen D, Hu P, Li W, Zhao D (2012) Direct imaging the Upconversion Nanocrystal core/shell structure at the subnanometer level: shell thickness dependence in Upconverting Optical Properties. Nano Lett 12(6):2852–2858. https://doi.org/10.1021/nl300421n
71. Liu L, Qin F, Zhao H, Lv T, Zhang Z, Cao W (2013) Shell thickness dependence of upconversion luminescence of β-$NaYF_4$:Yb, Er/β-$NaYF_4$ core-shell nanocrystals. Opt Lett 38(12):2101–2103. https://doi.org/10.1364/OL.38.002101
72. Märkl S, Przybilla F, Rachel R, Hirsch T, Keller M, Witzgall R, Mély Y, Wegener J (2024) Impact of surface chemistry of upconversion nanoparticles on time-dependent cytotoxicity in non-cancerous epithelial cells. Sci Rep 14(1):30610. https://doi.org/10.1038/s41598-024-83406-3
73. Rostami I (2021) Empowering the emission of upconversion nanoparticles for precise subcellular imaging. Nanomaterials 11(6):1541. https://doi.org/10.3390/nano11061541